Bathke, H., Sudhaus, H., Holohan, E., Walter, T. R., Shirzaei, M. (2013): An active ring fault detected at Tendürek volcano by using InSAR. - *Journal of Geophysical Research*, *118*, 8, 4488-4502

DOI: 10.1002/jgrb.50305

An active ring fault detected at Tendürek volcano by using InSAR

H. Bathke,[1] H. Sudhaus,[1,2] E.P. Holohan,[1] T. R. Walter,[1] and M. Shirzaei[3]

Received 21 December 2012; revised 15 July 2013; accepted 21 July 2013; published 16 August 2013.

[1] Although ring faults are present at many ancient, deeply eroded volcanoes, they have been detected at only very few modern volcanic centers. At the so far little studied Tendürek volcano in eastern Turkey, we generated an ascending and a descending InSAR time series of its surface displacement field for the period from 2003 to 2010. We detected a large (~105 km^2) region that underwent subsidence at the rate of ~1 cm/yr during this period. Source modeling results show that the observed signal fits best to simulations of a near-horizontal contracting sill located at around 4.5 km below the volcano summit. Intriguingly, the residual displacement velocity field contains a steep gradient that systematically follows a system of arcuate fractures visible on the volcano's midflanks. RapidEye satellite optical images show that this fracture system has deflected Holocene lava flows, thus indicating its presence for at least several millennia. We interpret the arcuate fracture system as the surface expression of an inherited ring fault that has been slowly reactivated during the detected recent subsidence. These results show that volcano ring faults may not only slip rapidly during eruptive or intrusive phases, but also slowly during dormant phases.

Citation: Bathke, H., H. Sudhaus, E. P. Holohan, T. R. Walter, and M. Shirzaei (2013), An active ring fault detected at Tendürek volcano by using InSAR, *J. Geophys. Res. Solid Earth*, *118*, 4488–4502, doi:10.1002/jgrb.50305.

1. Introduction

[2] Volcano ring faults present a twofold hazard, in that they can both generate sizable earthquakes [*Ekström*, 1994; *Shuler et al*., 2013] and act as eruption conduits [e.g., *Wilson and Hildreth*, 1997; *Holohan et al*., 2008]. On the other hand, they also can act as flow paths for ore-bearing hydrothermal fluids and hence represent mineral exploration targets [e.g., *Rytuba*, 1994]. Ring faults have been documented at ancient volcanic systems since the early 1900s [*Clough et al*., 1909] and mechanical explanations for their formation have been proposed since the 1930s [*Anderson*, 1936]. Although many volcanoes show the presence of ring structures, active ring faulting during phases of unrest at volcanoes is rarely observed.

[3] Active ring faults have been detected mainly in more recent decades, as volcanoes worldwide have become increasingly closely monitored in order to prepare for potential eruptions and related hazards. As summarized in Table 1, active ring faulting has been discovered at several volcanoes of varying compositions and has been inferred to have various modes of movement and a wide range of spatial dimensions. Such faulting activity has been detected and monitored mainly seismically and/or geodetically, either by instrument networks or by satellite. While the former provide temporally extensive but pointwise information, the latter enable spatially extensive measurement of surface displacement, even at volcanoes that are remote or otherwise difficult to access.

[4] Seismic methods have been used to detect blind ring fault activity during unrest or eruptive periods at the calderas of Rabaul [*Mori and McKee*, 1987], Campi Flegrei [*De Natale et al*., 2006], and Bárdarbunga [*Ekström*, 1994; *Fichtner and Tkalčić*, 2010]. At Fernandina [*Simkin and Howard*, 1970; *Filson et al*., 1973], Miyakejima [*Kumagai et al*., 2001], and Dolomieu [*Michon et al*., 2007], seismic evidence of ring fault activity was complemented by visual observations and, in the latter two cases, by tilt-meter and GPS data. At Sierra Negra [*Chadwick et al*., 2006; *Jónsson*, 2009], ring faulting was primarily detected through satellite-based Interferometry of Synthetic Aperture Radar (InSAR) data. Some of these detected ring faulting events occurred in conjunction with uplift (Rabaul, Campi Flegrei, Sierra Negra); others occurred in association with subsidence (Bárdarbunga, Fernandina, Miyakejima, Dolomieu).

[5] Common to all the above examples is that slip on the detected ring faults entailed surface displacement magnitudes of meters to hundreds of meters and occurred over a short time (day to weeks) during large eruptions and/or intrusions. At Tendürek volcano in Eastern Anatolia, however, we find indications that slip along ring faults can alternatively take place in conjunction with surface displacement of only several centimeters, can occur very slowly (over many years), and can lack clear evidence of contemporaneous intrusive or extrusive activity.

Additional supporting information may be found in the online version of this article.

[1]Department Physics of the Earth, Helmholtz-Centre Potsdam, GFZ German Research Centre for Geosciences, Potsdam, Germany.
[2]University of Potsdam, Institute of Earth and Environmental Sciences, Potsdam, Germany.
[3]School of Earth and Space Exploration, Arizona State University, Tempe, Arizona, USA.

Corresponding author: H. Bathke, Department Physics of the Earth, Helmholtz-Centre Potsdam, GFZ German Research Centre for Geosciences, Telegrafenberg, DE-14473 Potsdam, Germany. (bathke@gfz-potsdam.de)

2169-9313/13/10.1002/jgrb.50305

Table 1. Comparison of Volcanoes With Ring Fault Structures

Volcano	Direction of Surface Movement	Diameter of Ring Faults (km)	Method of Ring Faults Detection	Fault Orientation(s) and Slip Sense(s)	Duration and Cause of Activity	Amplitude of Surface Displacement (m)	References
Sierra Negra (Galapagos)	uplift	elliptic, 7 × 10	geodetic	outward inclined, reverse faulting, trapdoor like	several days, during repeating "trapdoor events"	1–3	*Chadwick et al.* [2006]; *Jónsson* [2009]
Rabaul (Papua New Guinea)	uplift	elliptic, 5 × 9	seismic, geodetic	inward and outward inclined	~2 years, during several eruptions	1.6	*Nairn et al.* [1995]; *Jones and Stewart* [1997]; *Saunders* [2001]
Campi Flegrei (Italy)	uplift/subsidence	circular, 12	seismic, geodetic, gravimetric	inward inclined	months-years, repeatedly during several eruptions	up to several meters	*Scarpati et al.* [1993]; *De Natale et al.* [2006]
Miyakejima (Japan)	subsidence	circular, 1.6	seismic, photographic	inward inclined, normal faulting	short, ~1 month, caldera collapse	~1,600–2,100	*Geshi et al.* [2002]
Dolomieu (LaRéunion)	subsidence	elliptic, 1.4 × 1	seismic, geodetic, photographic	inward inclined, normal faulting	short, ~1 day, caldera collapse	~330	*Michon et al.* [2007]
Fernandina (Galapagos)	subsidence	elliptic, 4 × 6.5	seismic, photographic	partly outward and inward inclined, normal and reverse faulting, trapdoor like	short, several days, caldera collapse	~300	*Simkin and Howard* [1970]
Bárdarbunga (Iceland)	subsidence	elliptic, 10 × 5	seismic	partly outward and inward inclined, reverse and normal faulting	short, several weeks	?	*Ekström* [1994]; *Konstantinou et al.* [2003]; *Fichtner and Tkalčić* [2010]
Tendürek (Turkey)	subsidence	elliptic, 10 × 14	geodetic	eventually inward inclined, normal faulting	long, hundreds of years	0.08	*Yılmaz et al.* [1998], this study

[6] Our findings were arrived at by analyzing two "small baseline subset" (SBAS) InSAR time series of displacement at Tendürek. These were derived from Envisat ASAR images for the ascending and the descending satellite tracks which spanned 2004 to 2009 and 2003 to 2010, respectively. The retrieved displacement velocity signal is dominated by a steady subsidence that is centered on the volcano summit. Analytical source optimizations reveal that the dominant part of the measured subsidence signal can be well simulated by a contracting subhorizontal, sill-like body.

[7] After removing the sill-related displacement component from the InSAR observations, we found a ring-shaped gradient in the residual velocity field. As validated by high-resolution RapidEye satellite images, this gradient coincides with an arcuate fracture system visible on the volcano surface. These observations indicate long-term slip on a subsurface ring fault at Tendürek.

2. Tendürek Volcano

2.1. Tectonic Setting

[8] Tendürek volcano is located in Eastern Turkey, where active regional tectonics relate to the ongoing north-south convergence of the Arabian and Eurasian plates and the associated westward "escape" of the Anatolian plate (Figure 1). This tectonic setting is generally characterized by north-south shortening and east-west extension [*Yılmaz et al*., 1998]. In the region around Tendürek, these strains are primarily accommodated by NE- or ENE-trending sinistral strike-slip faults and NW- or WNW-trending dextral strike-slip faults. Two of the latter, the Çaldıran and Balık Gölü faults [*Karakhanian et al*., 2004], lie immediately to the south and the north of the volcano, respectively. The region also hosts E-W trending folds and active thrust faults (e.g., the 2011 Van Earthquake), as well as N-S trending basins and normal faults. In addition, bends and/or steps along the strike-slip faults have locally resulted in uplifted ranges or pull-apart basins.

[9] Volcanism in the region began in the Late Miocene in association with the onset of the Anatolian plate's lateral escape [*Yılmaz et al*., 1998]. After peaking in the Pliocene, volcanic activity persisted through the Quaternary and into historical times. Historically active centers include Mt. Ararat, Tendürek, and Nemrut volcanoes [*Karakhanian et al*., 2002; *Simkin and Siebert*, 2002]. In the vicinity of Lake Van, various long-period seismic events have been recorded by local seismic networks [*Horasan and Boztepe-Güney*, 2006]. They suggest an upward movement of material, possibly magma or other fluids, and underline the magmatically and/or geothermally active nature of this region.

2.2. Geology

[10] A low-relief, polygenetic shield volcano, Tendürek reaches a height of about 3,580 m a.s.l. from a base of around 1,800 m. The edifice and its associated volcanic field measure approximately 30 km north to south and 20 km east to west (Figure 2). The edifice comprises two main cones, each with summit crater vents and many subordinate flank vents [*Yılmaz et al*., 1998]. Morphologically, the coalescence of the main cones causes an E-W elongation of the volcanic edifice.

[11] The basement rocks below Tendürek include Paleozoic meta-sediments, Cretaceous ophiolitic mélange, Paleocene marine limestones and flysch, as well as Late Miocene terrestrial

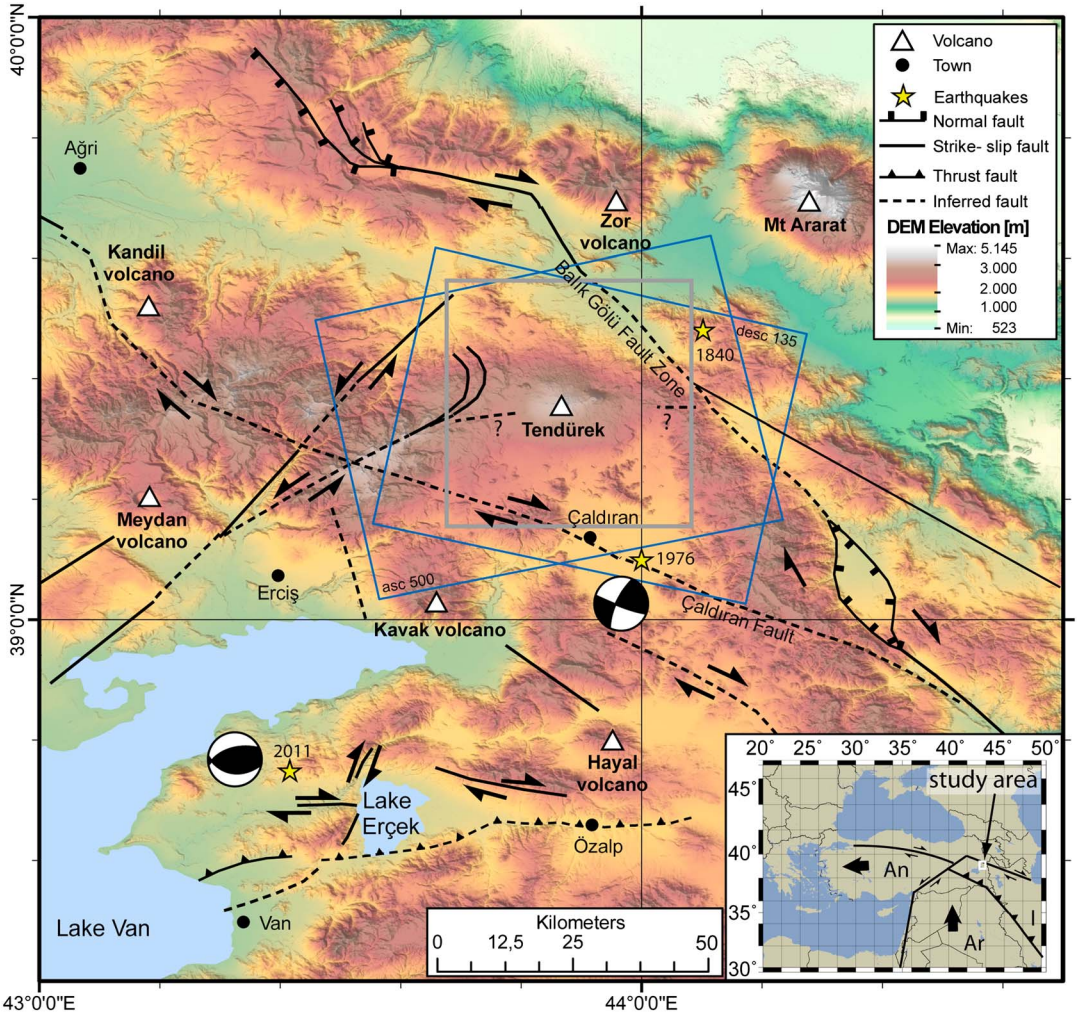

Figure 1. Volcanoes and structures of Eastern Anatolia in the vicinity of Lake Van modified after *Yılmaz et al*. [1998], *Karakhanian et al*. [2004], *Dhont and Chorowicz* [2005], and *Doğan and Karakaş* [2013]. The stars show the epicenters for the major seismic events in this region according to the NEIC catalog. The vertically oriented grey box marks the extent of Figure 2. The inclined blue boxes show the footprints of the Envisat satellite data. The small inset figure to the lower right shows Asia Minor and the major plate movements, modified after *Reilinger et al*. [2006]. The white rectangle outlines the investigated region in the east of Turkey.

sandstones and conglomerates [*Yılmaz et al*., 1998]. These reflect the progressive closure of the Tethyan Ocean, with emergence and uplift of the Anatolian region as the Arabian and Eurasian plates converged and collided. Alluvial deposits of the Çaldıran and Doğubeyazıt plains also underlie the Tendürek volcanic field at its distal edges in the north and south.

[12] Erupted materials are predominantly basaltic lavas, but these are interleaved with substantial trachyandesitic or trachytic lavas and pyroclastic deposits (flow and fall). Available radiometric dates for the main cones range from around 700,000–500,000 years BP to 13,000 BP [*Yılmaz et al*., 1998]. The youngest activity comprises small parasitic cones and basaltic lava flows formed along a N- S trending line at distances of up to 10 km to the northeast and the southeast of the main volcanic edifice. These youngest lavas are thought to have been produced around 2,500 years ago [*Yılmaz et al*., 1998].

[13] The two main cones are partly encompassed by an arcuate fracture system located on the lower flanks of the edifice. This arcuate fracture system cuts the southern half of the edifice, but is not visible in the northern half [*Yılmaz et al*., 1998]. It hence manifests as a half-ellipse with a 5 km long semi-minor axis and a 14 km long, E-W trending major axis.

[14] Tendürek is considered to be dormant, although its hydrothermal system powers local fumaroles and hot springs [*Ölmez et al*., 1994], *Karakhanian et al*., 2004]. An eruption or explosion at Tendürek may have occurred in 1855 [*Karakhanian et al*., 2002], however, and since the late 1970s there have been several reports of high fluorine concentration in local waters [*Oruc*, 2008]. These phenomena reveal the need to better understand the poorly known state of activity at this volcano and its subsurface structure.

3. Methods: Data Processing, Subsampling, and Modeling

[15] Constraints on the geometry and location of subvolcanic systems can be gained from studies of surface displacement [*Dzurisin*, 2007]. In situ instruments and on site investigations

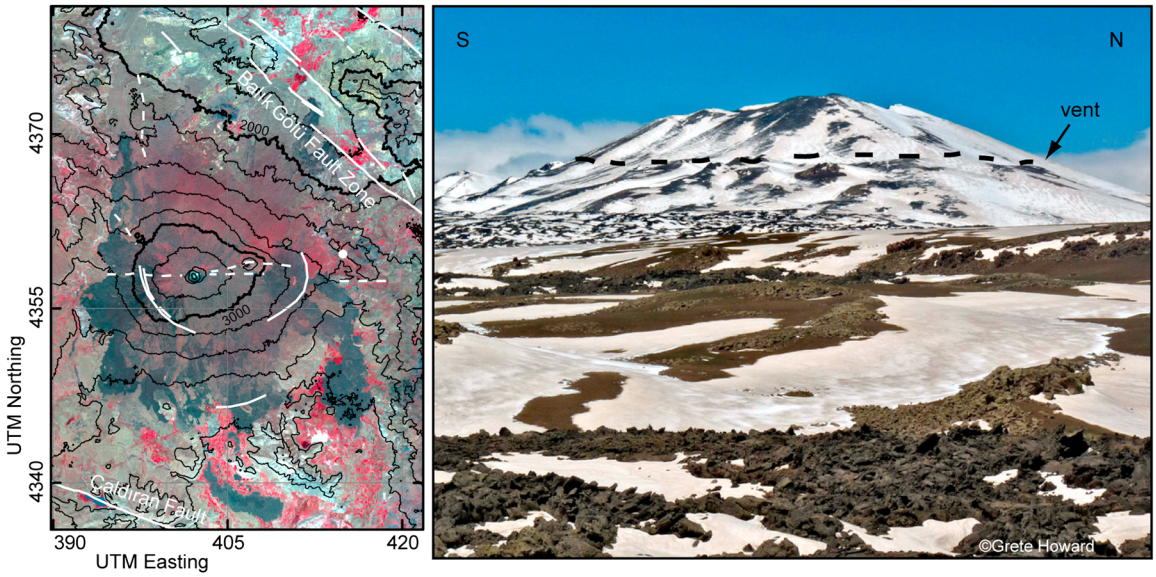

Figure 2. Left: RapidEye image from 30 August 2011 in false color (red, green, and blue channels are bands 5, 3, and 2, respectively; 5 m resolution). The red color marks vegetation and dark grey colors mark recent lava flows. Black lines show the contour lines of the digital elevation model with an interval of 200 m. The white lines mark inferred and mapped faults from *Yılmaz et al*. [1998]. The white dot marks the approximate location from where the picture (right) of Tendürek has been taken. Right: Photo of Tendürek volcano from 08 May 2009. The dashed black lines mark the arcuate fractures.

at Tendürek have also been very rare, however, due to political instability and the presence of minefields on the volcano [*Byrne et al*., 2009]. Consequently, surface displacement measurements made by using spaceborne SAR imagery can provide useful independent information for approaching these questions in this case. The following subsections describe the InSAR time series analysis, the data subsampling and error estimation, and the source modeling approach.

3.1. InSAR Time Series Analysis

[16] In the simplest approach, displacement at volcanoes can be derived from interferometry of two SAR images acquired at different times (two-pass interferometry). In cases where displacement magnitude is low, however, such as might be expected at a dormant volcano like Tendürek, simple two-pass InSAR may not yield any useful displacement signal. A more complex approach to detecting surface displacement at volcanoes is to generate an InSAR time series, whereby numerous SAR images taken over a longer time span are combined. One advantage of this approach is that it increases the signal to noise ratio, by for instance concentrating on temporally stable information and by facilitating the reduction of atmospheric artifacts. This enables the detection of even small displacements that occur over a longer time frame than is generally possible by using simple two-pass SAR interferometry alone. A second advantage is that the time series approach yields insights into the temporal evolution of displacement.

[17] To generate an InSAR time series for Tendürek, we combined 19 SAR images acquired by the ENVISAT satellite in the years from 2004 to 2009 in ascending track (track 500) and 22 images from 2003 to 2010 in descending track (track 135) (Figure 3). Time series generation involves making all possible two-pass interferograms from these data sets, selecting and combining those interferogram pixels with the best signal-to-noise ratio, filtering the interferometric phase signal to improve its quality, and finally converting the phase information to displacement in the line of sight (LOS) of the radar satellite.

[18] In detail, the processing chain for the InSAR time series involved the following steps, algorithms and software. For the SAR data focusing and interferogram formation, we used the software packages ROI_Pac [*Rosen et al*., 2004] and Doris [*Kampes and Usai*, 1999], respectively. To derive differential interferograms, i.e., to remove the phase contributions due to topography, we used the digital elevation model (DEM), derived from the shuttle radar topography mission (SRTM), at a resolution of ~90 m [*Farr et al*., 2007]. Differential interferograms have been filtered using a Goldstein adaptive filter [*Goldstein and Werner*, 1998]. We extracted the displacement signal from the interferograms and analyzed the temporal evolution of the displacement, by using the small baseline subset (SBAS) module in *StaMPS* [*Hooper*, 2008].

[19] *StaMPS* software uses interferometric phase shifts of identified stable pixels instead of complete interferograms. The stability of a pixel is evaluated based on its interferometric phase coherence and signal amplitude dispersion. For pixel selection, we used 53 small baseline interferograms in ascending orbit and 69 interferograms in descending orbit (Figure 3).

[20] For phase unwrapping, we used the minimum cost flow algorithm implemented in the *snaphu* software package [*Chen and Zebker*, 2001]. Spatially correlated phase contributions, i.e., turbulent atmospheric phase delay, and phase contributions due to orbital and DEM errors, can obscure any displacement-related signal. We removed these phase contributions by applying a low-pass filter in space and a high-pass filter in time to the unwrapped data [*Ferretti et al*., 2001; *Hooper*, 2006]. Furthermore, several independent interferograms from both satellite tracks confirm that the

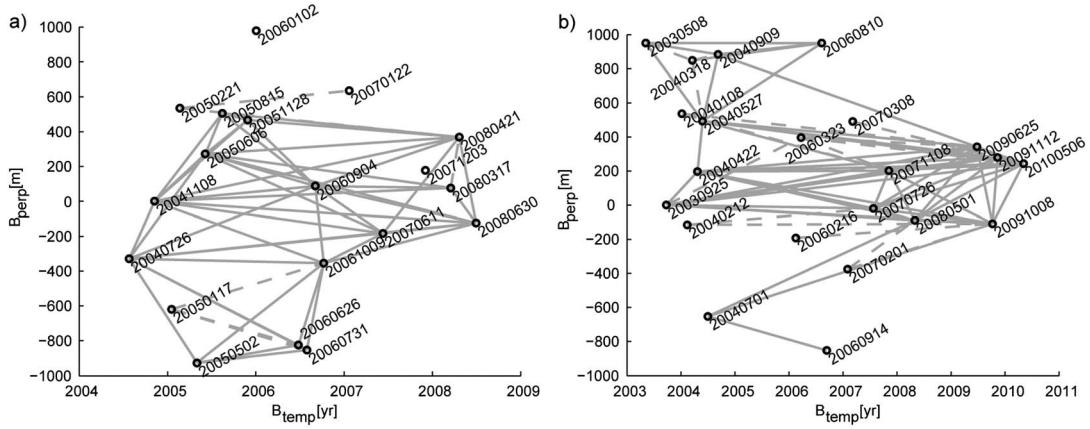

Figure 3. Diagram of temporal and perpendicular baselines for (a) 53 small baseline interferograms of the ascending track and (b) 69 interferograms of the descending track. Grey lines connect the dates of images (black circles) that form an interferometric pair in the time series analysis. Dashed lines mark images that have been discarded due to low signal-to-noise ratio.

measured signal is mainly related to ground displacement rather than to a topography-correlated atmospheric phase contribution [*Hanssen*, 2001] (Supplement S2, Supplementary Figures S6–S9). Our remaining signal is composed of surface displacement and reduced noise and can be used to determine the properties of its source.

[21] We discarded some interferograms from the time series due to their low signal-to-noise ratio. Finally, 47 interferograms in ascending mode and 52 interferograms in descending mode were used in the generation of the time series.

3.2. Data Subsampling and Error Estimation

[22] An InSAR time series typically contains several hundreds of thousands of data points, not all of which carry independent information. The analysis of such a data set can be made more efficient by reducing the number of data in an objective manner. The reduced data set will have data errors characteristics that differ from the original data set, however. Consequently, we empirically estimate the data errors of the original data set, and from this estimate we derive a weighting function for each point in the reduced data set. In that way, we balance the quality and distribution of the reduced, or subsampled, data set.

[23] In order to reduce the number of data points, we used the Quadtree algorithm [*Jónsson et al*., 2002]. We adjusted the algorithm's parameters, so that we ended up with about 2,500 pixels for each satellite track. After correction for atmospheric, orbital and topographic effects, any observed displacement in the InSAR time series will include some correlated and/or uncorrelated noise. To estimate the amount of such noise, we created sample variograms and covariograms from the full observational data set, by plotting the variance and covariance values of point-pairs, as a function of their separation [*Sudhaus and Jónsson*, 2009]. The data variance was estimated from sample semivariograms, at separations where the increasing variance values reach a stable plateau level (Supplement S1). The covariance was estimated by fitting a positive-definite function to the samples of each covariogram (Supplementary Figure S1). From the variance and the covariance functions, we built the data error variance-covariance matrix, such that the data points of each track were individually weighted in the later source optimization (see section 3.3).

3.3. Source Modeling and Optimization

[24] Surface displacement observed in InSAR time series at volcanoes is usually related to subsurface processes such as volume changes, migration of fluids, or movement on fractures. To investigate the characteristics of potential subsurface sources causing such displacement, we generally idealize the volcano system in terms of an analytical model. By changing the model's parameters in a statistically guided manner, we find the optimum model whose parameters best reproduce the surface displacement data.

[25] In our approach, we consider a magmatic or hydrothermal source of finite extent rather than a geologically more ambiguous point source. We have therefore implemented planar [*Okada*, 1985] and ellipsoidal [*Yang et al*., 1988] source models. We assumed a homogeneous elastic half-space with a Young's modulus of 33 GPa and a Poisson's ratio of 0.25. With these models, we ran a source optimization to estimate the parameters of those optimal sources that could best explain the observed displacement.

[26] We jointly optimized the ascending and descending data by using a Monte Carlo direct search method [*Sambridge and Mosegaard*, 2002], specifically a genetic algorithm [*Holland*, 1975]. This search algorithm starts with a chosen number of randomly drawn models and then explores the model parameter space for models with a "low cost"—i.e., with a good fit to the data. During the search, the parameters of preferably low-cost models are recombined to form a "next generation" of models, which again are evaluated, sorted, and selected by their cost. By doing this iteratively, the parameters of the models converge toward an optimum solution with lowest cost.

[27] To account for errors of the subsampled data sets in the source modeling, we weighted the residual observations, v, which constitute the difference between the observed and the synthetic modeled displacement, with the inverse of the empirically estimated data error variance-covariance matrix, $\boldsymbol{C}^{-1}$. Thus, the cost, f, in the optimization is given by:

$$f = \boldsymbol{v}_{\mathrm{asc}}^{T}\boldsymbol{C}_{\mathrm{asc}}^{-1}\boldsymbol{v}_{\mathrm{asc}} + \boldsymbol{v}_{\mathrm{desc}}^{T}\boldsymbol{C}_{\mathrm{desc}}^{-1}\boldsymbol{v}_{\mathrm{desc}}\,. \tag{1}$$

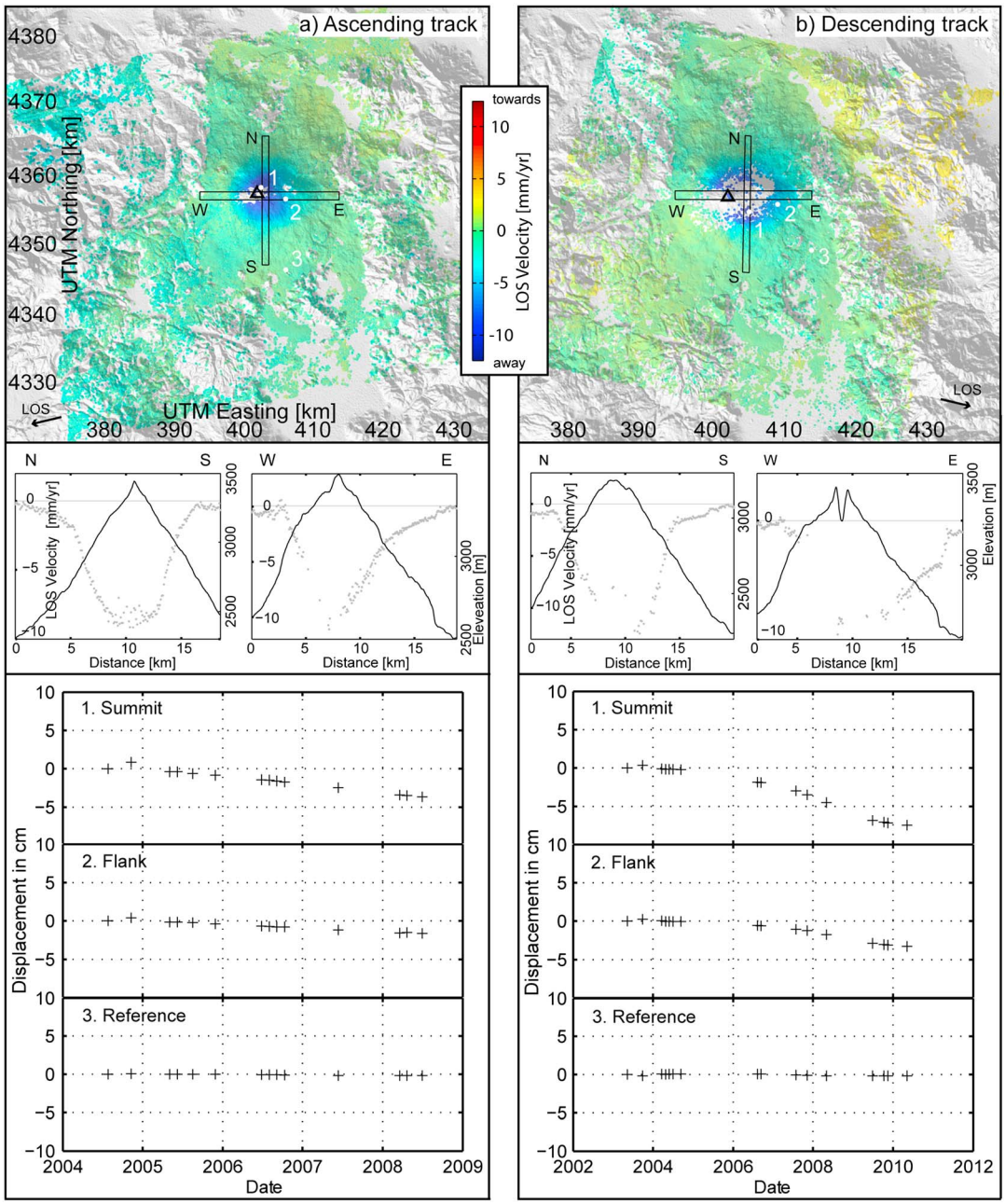

Figure 4. (top) Line of sight (LOS) displacement velocity from the SBAS time series analysis of the (a) ascending and (b) descending track satellite data. The black triangle marks the western crater at the summit of Tendürek volcano. (middle) Profiles along N-S and E-W of the LOS velocity (grey dots) and the surface elevation (black line). (bottom) Temporal changes of the mean of selected pixels within a circle of 200 m radius at the position of the white numbered points in the top panels.

[28] Several parameters control the performance of the search algorithm. *Population size* is the number of models in each generation from which, based on the *selection rate*, a fraction of the population with the lowest costs *f* are selected for the next generation. To explore a large solution space, a fraction of the selected solutions are also changed arbitrarily, based on the *mutation rate*. We chose a population size of 100, a selection rate of 0.5, a mutation rate of 0.7, and a generation number of 1000.

[29] To test the robustness of the model results with respect to errors of the subsampled data, we also created synthetic noise, based on the related error statistics [*Wright*, 2003; *Sudhaus and Jónsson*, 2009]. For each independent optimization run, new realizations of synthetic noise were added to the reduced data set, such that the data are slightly modified to reflect the data error. With these noise-modified data sets, we ran 200 independent optimizations and obtained a distribution of possible source models that explains the data well. To estimate 95% confidence intervals, and to allow for non-Gaussian model parameter distributions, we sorted the solutions of each model parameter and calculated the upper and lower 2.5% percentiles. From these model parameter distributions and the correlations between model parameters (i.e., model parameter trade-offs), we can learn about the uncertainties and non-uniqueness associated with our optimum subsurface deformation source.

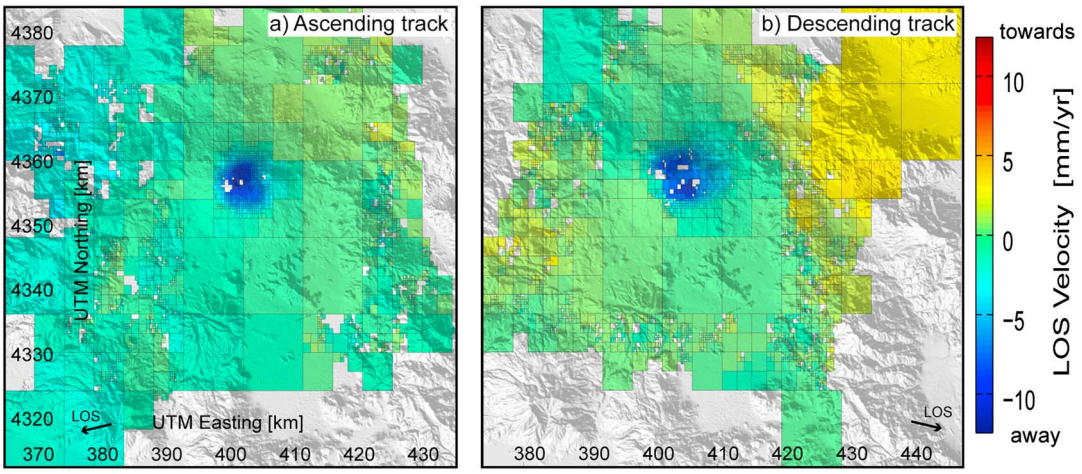

Figure 5. Results of data subsampling: Quadtree squares for (a) the ascending and (b) the descending tracks.

3.4. RapidEye Imagery

[30] Volcanic eruptions result in the generation of various types of erupted material, the deposition of which can be affected by preexisting geologic structures and morphological features. Mapping out the distributions of deposits of different types may therefore reveal the locations of older geologic structures. In this way, high-resolution multispectral satellite data, which allow one to differentiate deposits of different chemical composition, may also enable one to map lineaments and fractures at surface.

[31] We used six RapidEye image tiles (25 × 25 km) dating from 30 August 2011. These have five spectral bands (three visible, two near infrared) and a 5 m spatial resolution. To easily identify lava flows from their surroundings, we produced a false color image by using the bands 5, 3, and 2 for the red, green, and blue channels, respectively. From

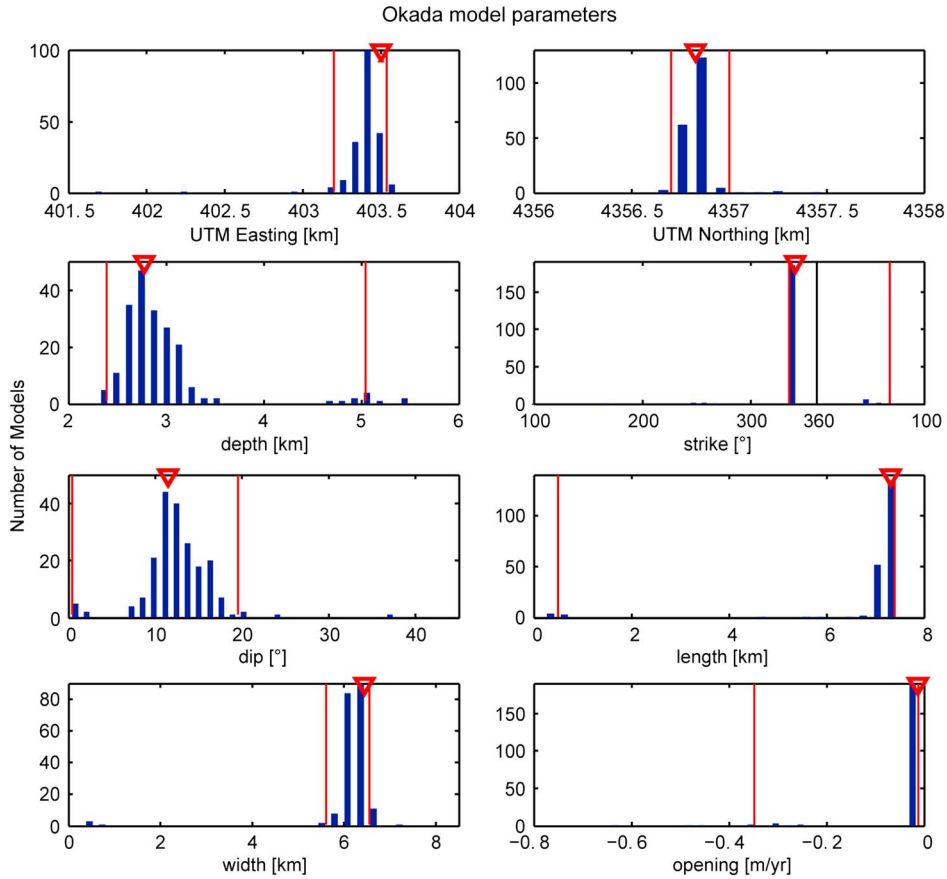

Figure 6. Histogram of 200 independent optimization results for the Okada model parameters. Note that as input for the results here and in Figure 7 we used the Quadtree subsampled data. Triangles give the corresponding optimum values and the red vertical lines mark the 2.5 and 97.5% percentile.

Table 2. Optimization Results: Parameters for the Okada and the Yang Source Models

Okada Source				Yang Source			
Source Parameters	Opt. Solution	Percentile (2.5% 97.5%)		Source Parameters	Opt. Solution	Percentile (2.5% 97.5%)	
UTM Easting [km]	403.5	403.2	403.5	UTM Easting [km]	403.5	402.8	403.7
UTM Northing [km]	4356.8	4356.7	4357.0	UTM Northing [km]	4356.8	4356.4	4357.1
Depth [km] w.r.t. mean elevation (1.9 km)	2.7	2.3	5.0	Depth [km] w.r.t. mean elevation (1.9 km)	3.6	3.4	4.8
Strike [°]	341	335	68	Strike [°]	215	35	308
Dip [°]	11	1	20	Plunge [°]	3	~0	35
Length [km]	7.3	0.5	7.4	Major axis [km]	4.7	1.4	4.9
Width [km]	6.4	5.6	6.6	Axis ratio b/a	0.07	0.06	0.46
Opening [cm/yr]	−1.4	−1.4	−34.9	Pressure change [GPa]	−0.012	−0.018	−0.001

this high-resolution image, we can then identify by eye differences in volcanic deposits and map structures around the volcanic edifice.

4. Results: InSAR Time Series and Modeling

4.1. Displacement Velocity Field at Tendürek

[32] The InSAR time series shows that Tendürek volcano underwent gradual subsidence between 2003 and 2010 (Figure 4). Displacement rates in radar line of sight are near linear in the ascending data set (Figure 4a) and slightly nonlinear in the descending data set (Figure 4b). As first-order approach, we therefore separately calculated a linear (i.e., average) velocity of the observed signal for each track. The subsidence velocity reaches a maximum rate of 11 mm/yr at the volcano summit. This subsidence rate decreases to about 6 mm/yr on the upper volcano flanks and to about 2 mm/yr on the lower volcano flanks, where it is similar to the data noise level (see Supplementary Table S1).

[33] The shape of the signal in the ascending track is slightly elliptical to almost circular (diameter ~10 km) (Figure 4a, top panel), whereas that in the descending track is more clearly elliptical in an E-W direction (major and minor axes of 14 × 10 km) (Figure 4b, top panel). Profiles through the signal show a bowl-shaped pattern at the volcano summit that continues with a smaller gradient toward the lower eastern volcano flanks (Figure 4, middle panels). This gradient is weak in the E-W oriented profiles of the ascending track

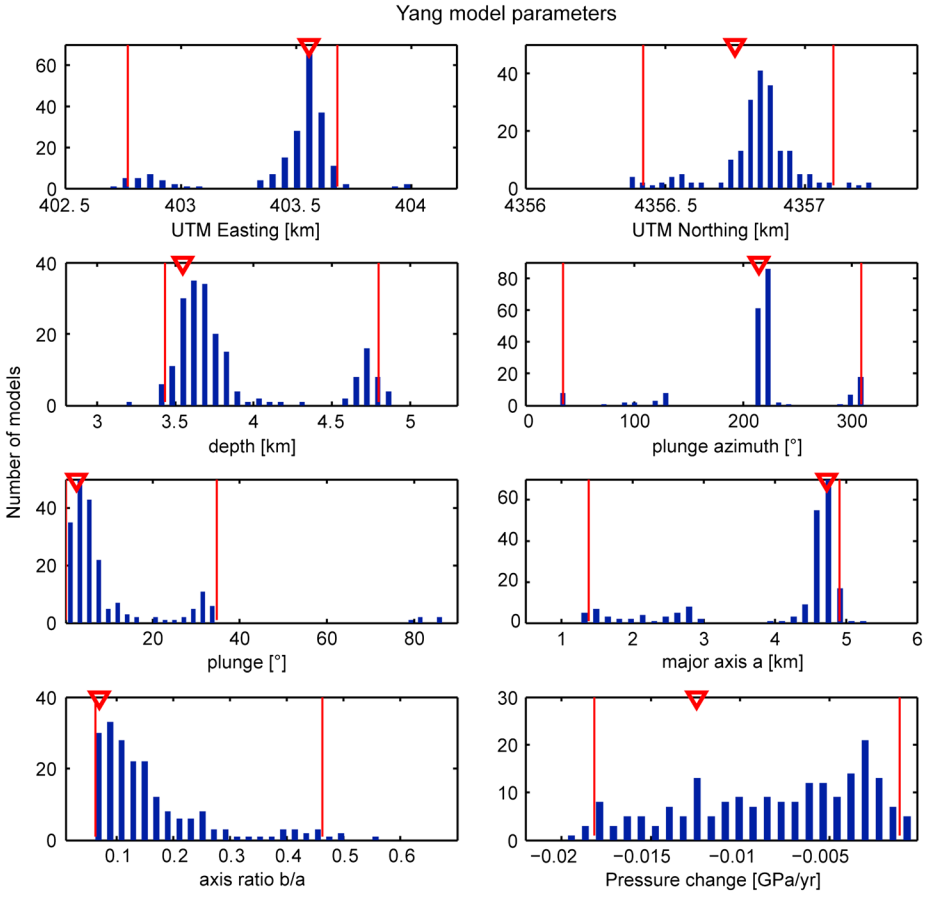

Figure 7. Histograms of 200 independent optimization results for the Yang model parameters. Triangles give the corresponding optimum values and the red vertical lines mark the 2.5 and 97.5% percentile.

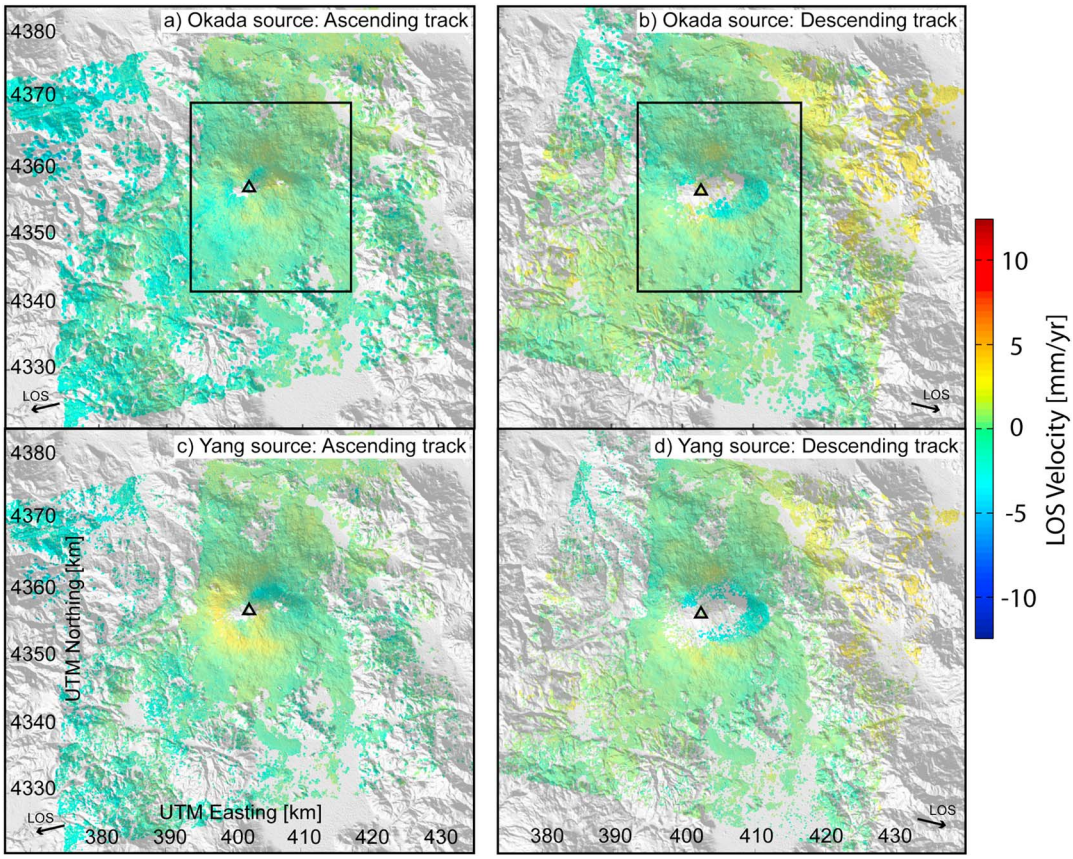

Figure 8. Residual displacement velocity of the optimum Okada source model for (a) the ascending and (b) the descending tracks and of the optimum Yang source model for (c) the ascending and (d) the descending tracks. The black boxes in Figures 8a and 8b mark the extent of the area enlarged in Figure 9.

compared to a strong gradient in the E-W oriented profiles of the descending track. These apparent differences in signal pattern likely arises from the different satellite viewing geometries. Nevertheless, the area of subsidence covers ~105 km^2, lies above 2,600 m a.s.l., and is elliptical in both ascending and descending satellite tracks.

4.2. Source Modeling of the Tendürek Subsidence Signal

4.2.1. The Subsampled Data Set

[34] As is typical for volcanoes, the pixel distributions in our data sets are heterogeneous (Figure 4). Due to rough topography and snow coverage, there are only a few stable pixels at the volcano summit and in the far-field region (at distances greater than c. 20 km). In contrast, there are many stable pixels on the flanks of the volcano. The Quadtree square distribution (Figures 5a and 5b) compensates for this heterogeneity by having a denser sampling of pixels at the summit and in the far field (compared to the original data set), whereas sampling of pixels on the flanks is sparser. We used these subsampled, or reduced, ascending and descending data sets for the modeling, results of which are presented in the next subsections.

4.2.2. Okada Source Model Results

[35] The best fitting Okada plane lies below the center of the main volcano summit and dips gently toward the northeast. This optimum Okada plane measures 6 × 7 km, is centered at UTM easting 403.5 km and UTM northing 4356.8 km, lies at a depth of 2.7 km, strikes at 340°, dips at 11°, and closes at 1.4 cm/yr. This result has an estimated total volume change of ~$4.55 \cdot 10^{-3}$km^3.

[36] The dip and depth of the model plane are the least well constrained, since here we find bimodal parameter distributions. The other parameters are well constrained, however, as shown by the histograms with pronounced peaks and narrow confidence intervals (Figure 6 and Table 2). The optimization results for Okada source models are therefore generally robust.

[37] Two-dimensional correlations of the Okada source parameters are provided in Supplementary Figure S2. They show that solutions change significantly when the strike changes from northwest to northeast (i.e., when the origin of the Okada plane differs). Moreover, as depth increases, the dip increases, the length shortens, and rate of closure increases.

4.2.3. Yang Source Model Results

[38] The best fitting Yang ellipsoid is also centered below the volcano summit, and it is almost horizontal with a very gentle plunge toward the SW. This optimum ellipsoid measures 4.7 × 0.33 km, is centered at UTM easting 403.5 km and UTM northing 4356.8 km, lies at a depth of 3.6 km, has a plunge azimuth of 215° and a plunge angle of 3°, and undergoes a pressure change of −12 MPa/yr. This result has an estimated total volume change of ~$3.29 \cdot 10^{-3}$km^3.

[39] The optimizations of the Yang source model are generally less robust, however. The histograms (Figure 7) and the parameter correlations (Supplementary Figure S3) for the Yang source show that there are three major peaks in

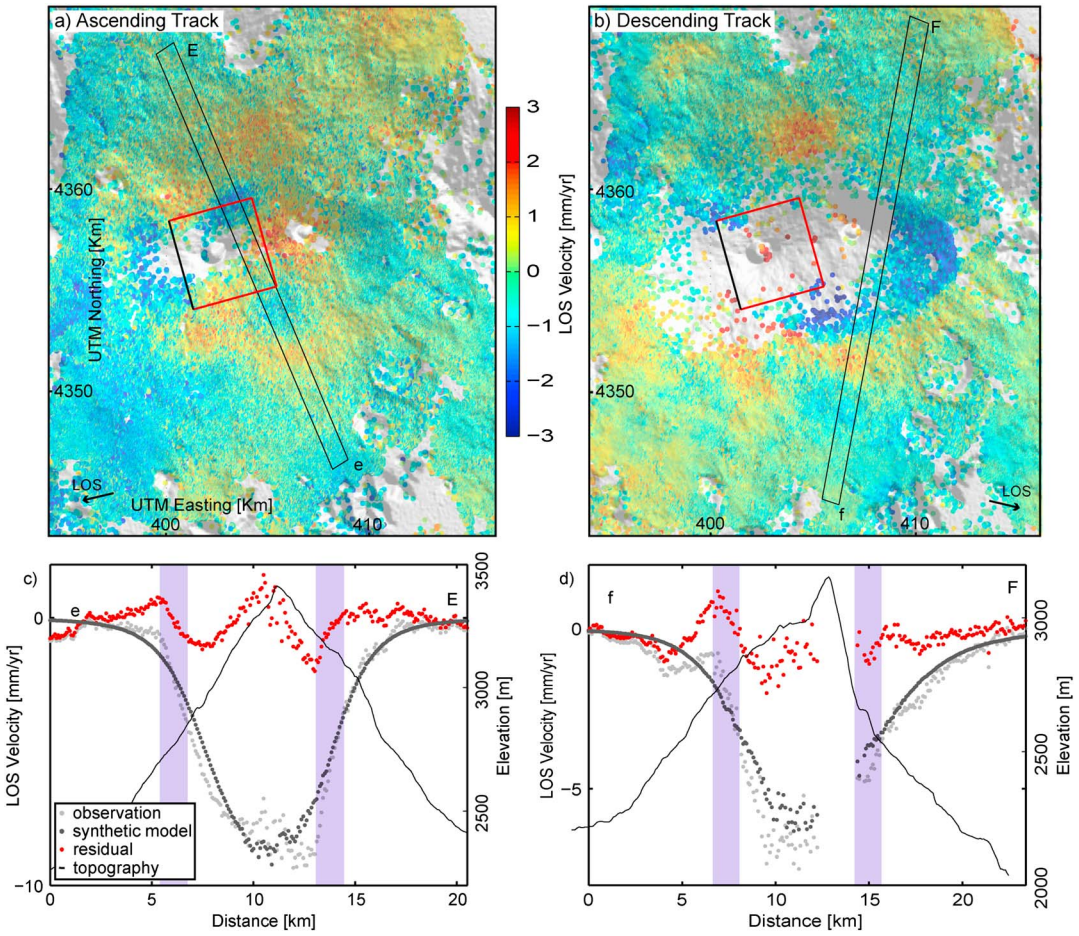

Figure 9. (a and b) Zoom into residual displacement velocity maps and (c and d) profiles. The red rectangles in Figures 9a and 9b show the position and lateral dimensions of the optimum Okada source model (upper edge in black). The black rectangles through the volcano show the position of residual velocity profiles given in Figures 9c and 9d. These profiles are chosen to illustrate regions with strong gradient in the residual deformation. Light grey points give the observed line of sight displacement velocity, dark grey points show the synthetic displacement velocity of the inferred Okada plane, and the red points mark the residual. The solid black line represents the elevation of the surface of the volcano. The vertical blue bars mark the inferred surface location of the arcuate fracture system.

most of the source distributions (UTM easting, UTM northing, plunge azimuth, plunge, major axis). They show that an ellipsoid at 3.5–4 km depth, with a nearly horizontal major axis length of 4–5 km, explains the displacement almost as well as a shallower ellipsoid at a depth of 3.2–3.5 km and with a vertical major axis length of ~1 km (Table 2). A third solution is an even deeper source located at a depth of 4.5–4.9 km, with an ill-constrained major axis length. These solutions deviate in their plunge azimuth also. The optimum solution with an almost horizontal plunge has, due to the axis symmetry of the ellipse, two peaks in the distribution of the plunge azimuth, at about 30° and 220°. Other less likely solutions tend to group at near-perpendicular plunge azimuths of 130° and 310°. Overall the pressure change is very poorly constrained and ranges from 1 to 20 MPa/yr.

4.2.4. Analysis of Residual Displacements

[40] Residual displacements can provide further insight into processes that contribute to the signal but are not incorporated into our model. These are obtained through subtracting the displacement predicted by the optimum source models from the observed surface displacement (Figure 8).

[41] The vertical displacement component of our sill model can explain most of the observed signal, whereas the horizontal displacement component shows larger residuals (Supplementary Figure S4). The vertical and horizontal displacement components of our ellipsoidal model both show large spatially correlated residuals (Supplementary Figure S5).

[42] The residual displacement in the ascending and descending data generally does not exceed 3 mm/yr for the Okada model and 5 mm/yr for the Yang model. Therefore, these models explain the majority of the observed displacement signal.

[43] Nonetheless, a systematic ring-like pattern is seen in maps and profiles of the residual displacement velocity field (Figure 9). In the ascending track, we identified an ellipsoidal boundary, where a gradient in the displacement of up to some millimeters is evident (Figures 9a and 9c). In the descending data (Figures 9b and 9d), we found pronounced discontinuities, rather than gradients. These coincide with Tendürek volcano's arcuate fracture system [*Yılmaz et al.*, 1998] (Figures 10a and 10b).

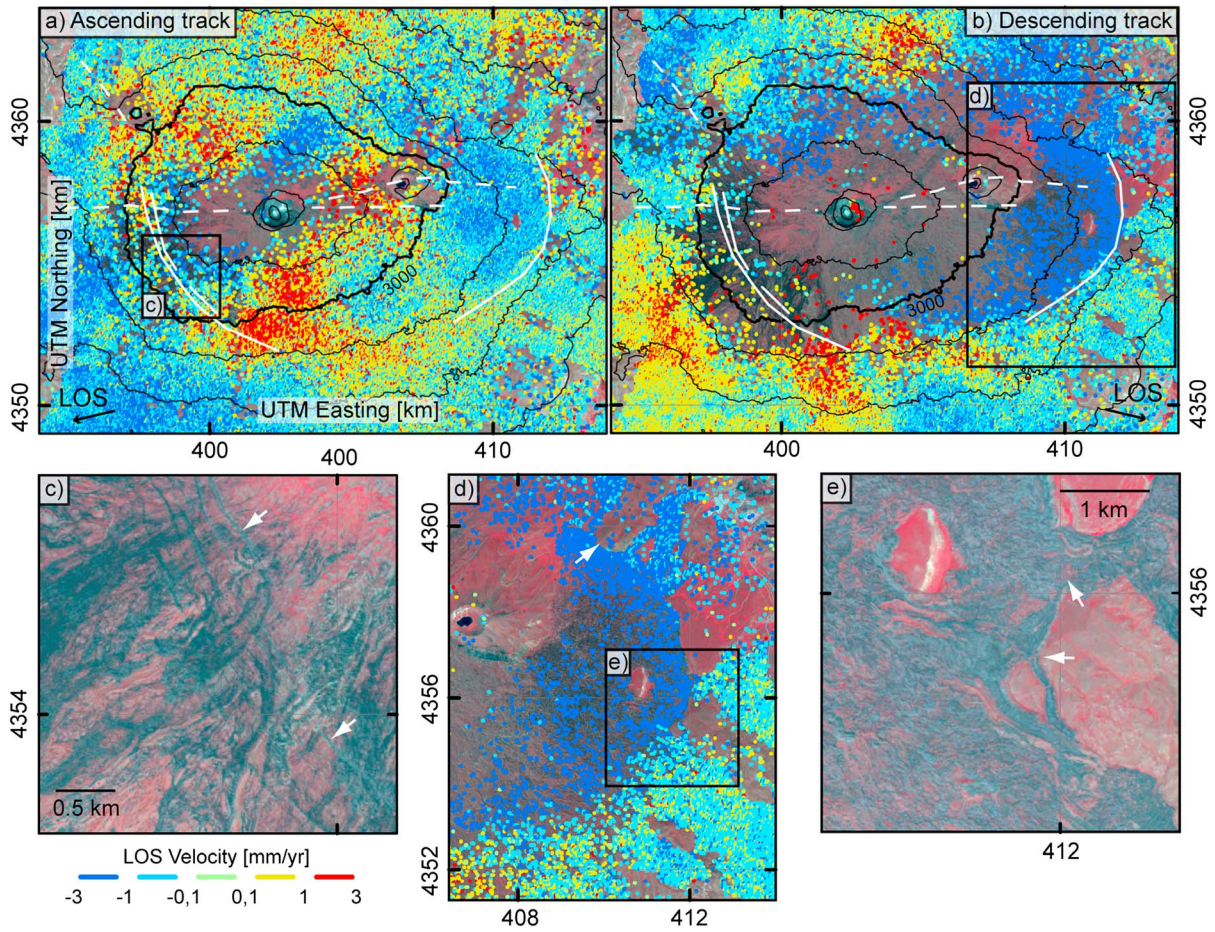

Figure 10. RapidEye image in false color (see also caption to Figure 2) with overlays of residual displacement velocity of the (a) ascending and (b) descending tracks, and of observed or inferred fractures (solid or dashed white lines) at Tendürek volcano, from *Yılmaz et al*. [1998]. Black lines show the contours from the digital elevation model with an interval of 200 m. (d) Enlarged box of the descending residual velocity. The white arrow shows the location of a small eruptive vent. (c and e) Enlarged images of the southwestern and eastern volcano flanks, in which white arrows indicate arcuate fractures and places where the migration of a lava flow has been guided by the previously existing arcuate fractures.

4.3. Surface Features in RapidEye Data

[44] In the false color image of the RapidEye data (Figures 2 and 10), vegetation is shown in red and recent lava flows are shown as shades of dark grey. In this image, we note several features of interest related to the arcuate fracture system surrounding the volcanic edifice. First, the system comprises several subparallel lineaments on the southwestern flank (Figure 10c). These are up to ~6 km long and are concentrated in a ~1.3 km wide region. Second, there is a small volcanic vent located directly on the continuation of the arcuate fracture system (Figure 10d). Third, the arcuate fracture system appears to have acted as a barrier to some of the youngest lava flows in the southeast (Figure 10e).

5. Discussion

[45] Our InSAR time series shows not only that the so far little studied Tendürek volcano subsided, but also that this surface displacement was partly controlled by an arcuate fracture system on the volcano flanks. From 2003 to 2010, Tendürek underwent a maximum subsidence of 7–8 cm, within an elliptical area of 10 × 14 km and with a steady, near-linear velocity of 11 mm/yr.

[46] For the period of 1993 – 2000, an unpublished two-pass interferometric study (M.Sc. Thesis) by *Tolluoglu* [2006] reported a maximum subsidence of about 12–15 cm at the volcano summit. This corresponds to a rate of 15–19 mm/yr, which has a similar signal magnitude to the subsequent subsidence detected in our study. Consequently, we conclude that subsidence at Tendürek has likely been ongoing since at least 1993.

[47] Analytical source modeling of the detected signal is most consistent with, and mostly explained by, a deflating sill-shaped deformation source. The residual displacements show a strong gradient along the location of the arcuate fracture system (Figures 10a and 10b). In the following sections, we discuss the assumptions and restrictions of the applied methods, possible explanations for the observed subsidence signal, and the context of our interpretation with respect to active ring faulting at modern volcanoes.

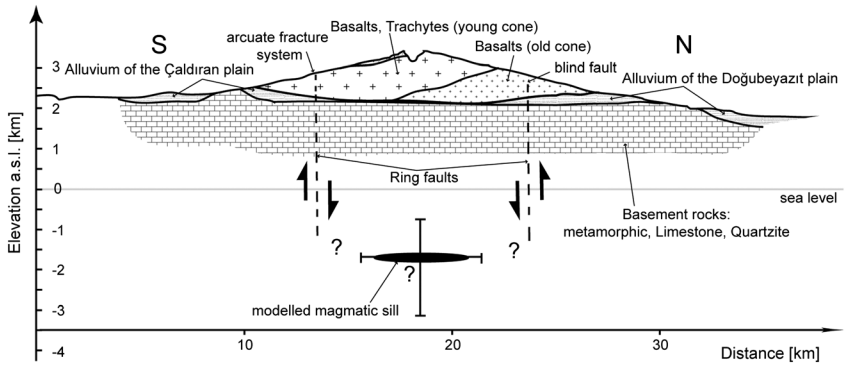

Figure 11. Schematic cross section of the source of deformation and the inferred ring fault system at Tendürek volcano (vertically exaggerated by a factor of 2). The dip angle of the ring fault is speculative, as indicated by question marks, and therefore the ring fault is drawn vertically by convention. The internal structure of the edifice and the basement is schematic. Surface geology is taken from *Yılmaz et al*. [1998].

5.1. Modeling Assumptions

[48] Our modeling gives insight into the subsurface processes that could have caused the observed signal. Nevertheless, as in any such study, there are some model assumptions that are unlikely to be true in nature and that, if changed, could in detail lead to some differences from the modeling results presented.

[49] The main a priori assumptions here are that topography, crustal heterogeneities, and secondary deformation sources are negligible when modeling the dominant deformation source. For topography, *Cayol and Co*rnet [1998] showed that displacement on volcanoes with slopes higher than ~20° differs significantly from estimations made assuming a half-space. The average slope of Tendürek is only about 7°, however, and therefore the role of topography is ignored by us in this case. The absence of crustal heterogeneities in our model is also justified, because without appropriate constraints, a more complex model setup would have resulted in larger model parameter ambiguities. Following analysis of residuals, the assumption of no secondary deformation source was found to be not strictly justified. As discussed below, however, this secondary source appears to be a ring fault, implementation of which into our modeling scheme is complex and beyond the scope of the present study.

[50] A further minor a priori assumption here is that the deformation source exhibits a uniform displacement along its boundary (e.g., uniform closing along the Okada plane). We also tested distributed opening along our optimum Okada plane; however, this does not improve the model fit significantly. In the absence of better geological constraints, a more complex source dislocation pattern therefore does not improve the understanding of the source mechanisms at Tendürek volcano, and so we decided that adopting the simpler source is the better solution.

5.2. Interpretation of the Main Deformation Source at Tendürek

[51] The observed displacement velocity can be reasonably well explained with a range of Yang or Okada source models, rather than just through one precise optimum solution (Table 2). Nevertheless, the Yang source models lead to higher residual displacements than the Okada source models (Figure 8). Therefore, we considered the Okada model to be more suitable for explaining the measured displacement. Surface displacement data alone is not sensitive to distinguish between a sill-like source from a flat-topped reservoir [*Yun et al*., 2006]. Therefore, our best fit sill-like source could also resemble the flat roof of a more vertically extensive body.

[52] In the following paragraphs, we consider three geological phenomena that commonly cause deformation at volcanoes and hence could be represented by the inferred deformation source model.

[53] A first common deformation mechanism is spreading or sagging of the volcano edifice under gravity. Spreading would result in outward directed horizontal motion on the volcano flanks, whereas inward horizontal motion is observed (Figures S4 and S5). Moreover, both spreading and sagging require a layer of soft and weak material for the volcano to sag into or slide along [e.g., *Byrne et al*., 2013, and references therein]. The most obvious candidates for such a layer at Tendürek are the recent alluvial sediments. These outcrop at the volcano base between 1.8 and 2.3 km a.s.l. and have thicknesses of less than 200 m [*Yılmaz et al*., 1998]. Our modeling results show that the deformation source lies at a 0.8–3.1 km b.s.l (Figure 11). Consequently, we discard spreading or sagging as potential deformation processes at Tendürek over the period of observation.

[54] A second possible deformation mechanism is hydrothermal activity. This occurs at Tendürek, as evidenced by fumarolic activity [*Ölmez et al*., 1994], and can cause surface subsidence through surface discharge or subsurface withdrawal of fluids. In addition, alteration and weakening of rock masses by hydrothermal activity can lead to their easier compaction and deformation [*Cecchi et al*., 2004], potentially also resulting in subsidence at the volcano.

[55] A third possible source for the subsidence at the surface is volume loss arising from the cooling, solidification and degassing of a subsurface magmatic body. The total volume reduction based on our optimum source models is around $3.29 - 4.55 \cdot 10^{-3}\mathrm{km}^3$ with an annual rate of $0.47 \cdot 10^{-3}\mathrm{km}^3$/yr or $0.65 \cdot 10^{-3}\mathrm{km}^3$/yr for the Yang or Okada sources, respectively. The complete solidification of a basaltic melt with a density of 2,600 kg/m^3 to solid gabbro with a density of 2,800–3,100 kg/m^3 causes a volume reduction of around 7–16% [*Sigmundsson et al*., 1997; *Shirzaei et al*., 2013]. The solidification of more evolved melts (e.g., trachytic or granitic) results in even higher volume reductions of 18–25% [*Sigurdsson*, 2000]. From the assumptions that the potential magma body below Tendürek measured 6 × 7 km (as indicated by our best

fit sill-like model) and that it had a conservative thickness of 50 m, its initial volume was 2.1 km^3. This means that a 0.2% volumetric change of this body would match the estimated absolute volume change of the source. Therefore, a partial solidification of the magmatic body, interlinked with volume reductions due to associated cooling and degassing, could comfortably explain the observations.

5.3. Tectonic Influence

[56] Several features of the Tendürek volcanic field are consistent with formation under a tectonic regime of north-south shortening and east-west extension (Figure 1) [*Reilinger et al*., 2006]. These include a N-S alignment of several parasitic cones in the east of the volcanic field and a N-S trending fissure in the west, which presumably reflect the preferred orientation of regional dykes [*Yılmaz et al*., 1998]. The E-W elongations of the volcanic edifice and of the arcuate fracture system are not obviously consistent with such as regional dyke control, however. Similar perpendicular alignment of the long axis of the displacement field to the regional dyke orientation was observed in the Lazufre volcanic field, South Andes [*Ruch and Walter*, 2010]. Maximum horizontal compressive stress perpendicular to the elongation of the displacement field can explain these patterns following the borehole breakout theory [*Ruch and Walter*, 2010]. A similar concept might apply as well at Tendürek volcano.

[57] Alternatively, the orientations of the edifice and the arcuate fracture system could relate to control on magma pathways from a regional fault. *Yılmaz et al*. [1998] map an east-west trending fault on the eastern side of the volcano (Figures 1 and 2), which, if projected westward along strike, passes through the main craters, as well as the long axes of both the edifice and the arcuate fracture system. To the east, this fault appears to link into the Balık Gölü fault, and thus may well be a part of the highly active regional tectonic system.

5.4. An Active Ring Fault at Tendürek Volcano

[58] The arcuate fracture system on Tendürek volcano coincides with systematic gradients in the residual displacement velocity maps (Figures 10a and 10b). Although this fracture system has developed only around the southern half of the volcano, the associated residual displacement gradients also appear around the north of the volcano (Figures 10a and 10b). This means that the arcuate fracture system most likely represents the trace of a subsurface fault that forms a complete ring around Tendürek volcano.

[59] That the surface expression of the ring fault is better developed on one side of the volcano (Figures 2 and 10) is commonly observed in analog and numerical models of ring fault formation [e.g., *Roche et al*., 2000; *Holohan et al*., 2011], as well as at volcanoes in nature [*Lipman*, 1997] ("Trapdoor"-like subsidence—Table 1). A geodetic observation consistent with larger slip in the south and west of the ring fault is that the horizontal component of the residual displacements within the ring structure is dominantly westward (Figures S4 and S5). This is in agreement with recent analog models that show unidirectional horizontal displacements of caldera floors, directed toward the area of inferred maximum slip along the ring fault [*Holohan et al*., 2013]. By adopting this concept to the Tendürek ring fault, one may hypothesize that the ring-fault's slip is greatest, and hence its surface expression is clearest, in the south west.

[60] The orientation of the ring fault is not constrained in this study and is hence depicted as vertical in Figure 11. Consequently, whether the ring fault and the sill-like deformation source are linked remains an open question. One could assume that the ring fault connects the arcuate fracture system at surface to the edge of the inferred sill-like source over a vertical distance of 3.4–6.1 km (Figure 11). If so, then along a N-S cross section, where the source and arcuate fracture diameters are 6 km and 10 km, respectively, the fault dip is inward at 60–72°. Along an E-W profile, where the source and arcuate fracture diameters are 7 km and 14 km, respectively, the ring fault dip is inward at 44–60°. Even if there is no geometric linkage between the ring fault and sill, its peripheral location from the subsidence source points to the ring fault being inward inclined and normal. This is evident from analog and numerical models of ring fault formation [e.g., *Roche et al*., 2000; *Holohan et al*., 2011]. In this case, the sill and the ring fault have a kinematic linkage.

[61] Another outstanding question is whether the ring fault and the inferred sill-like source are genetically related. At Rabaul volcano (Table 1), for example, the active ring faults were generated during a major subsidence and eruption event many centuries prior to their reactivation during a recent uplift event. In this case, the magma body causing reactivation of the ring faults was very unlikely to be genetically linked to the ring fault's formation [*Saunders*, 2001]. A similar scenario may have occurred at Tendürek, for several reasons. First, the aspect ratios of the inferred sill-like source and the arcuate fracture system are quite different (1.17 vs. 1.4). Second, they are off-centered from each other (Figure 9). Third, the optical data indicate that the arcuate fractures, and hence the underlying ring fault, were formed at least 13,000 years ago [*Yılmaz et al*., 1998], as they are crosscut by lava flows from the summit (Figure 10e). Fourth, inward inclined normal faults may lead to a space problem at depth during subsidence [*Branney*, 1995]. Therefore, (a) fault geometry at depth is more complicated, or (b) the reservoir size during the formation of the ring faults has been significantly larger than today, leading to a more vertical or even outward dipping ring fault geometry. The Tendürek ring fault may hence have been generated much earlier, either in a collapse event or an uplift event, and reactivated during the slow subsidence that occurred in the period of our observation.

[62] Activity along ring faults is usually observed during catastrophic events or "unrest" periods at volcanoes (Table 1, references therein). For example, active ring faults have been detected or observed during collapse caused by magma withdrawal (Miyakejima, Dolomieu, Fernandina) and during uplift caused either by magma intrusion (Rabaul, Sierra Negra) or possibly also by hydrothermal activity (Campi Flegrei). The durations of these events ranged from several days to months, and the magnitudes of the associated surface displacement ranged from several meters to several hundreds of meters (Table 1). In contrast, the duration of ring fault activity at Tendürek volcano was at least eight years and possibly several decades, and the magnitude of associated surface displacement was on the order of several centimeters. Moreover, Tendürek volcano was apparently dormant during this time, and so there is no obvious link to concurrent magma intrusion or withdrawal. Our study at Tendürek therefore provides an alternative example of long-term slip along ring faults that, as proposed by *Walker* [1984], is driven by processes other than rapid magma intrusion or withdrawal.

6. Conclusions

[63] InSAR-derived measurements show that Tendürek volcano has subsided continuously between 2003 and 2010. The maximum detected subsidence over this period was 7–8 cm, corresponding to a rate of 11 mm/yr.

[64] The linear part of our observed subsidence signal can be best explained by a near-horizontal, contracting, sill-like body that lies at a depth of 0.8–3.1 km b.s.l. and that has lateral dimensions of about 6 × 7 km. The body's total estimated volume change over the eight year observation period is $\sim 4.55 \cdot 10^{-3} km^3$. Sagging or spreading of Tendürek volcano is an unlikely deformation mechanism, as the required weak sedimentary layers are located at a much shallower depth than the modeled source. Partial solidification of a sill or flat-topped reservoir can more readily explain the modeled volume change, although contributions to this from cooling, degassing, and/or hydrothermal activity cannot be excluded.

[65] The residual displacement field shows gradients coinciding with an arcuate fracture system that is only developed on the southern flank of Tendürek volcano. These displacement gradients also continue around to the northern flanks, however, and so form a complete ellipse around the volcano. These gradients and the associated arcuate fracture system likely represent the surface expression of slip on a blind ring fault that encircles Tendürek volcano.

[66] From optical data, we find that basaltic lava flows from the summit cross and bury parts of the arcuate fracture system on the eastern flank of the volcano. Although the absolute age of these lavas is poorly constrained, they are probably at least 13,000 years old [*Yılmaz et al*., 1998]. The arcuate fracture system, and consequently the ring fault, must thus be older than this age. As seen at other volcanoes, for example Rabaul [*Saunders*, 2001], the ring fault at Tendürek is therefore probably an inherited structure that has been reactivated during the recent hydrothermal or magmatic activity at the volcano.

[67] Finally, our study of Tendürek volcano shows that ring faults may slip not only due to magma movements and catastrophic eruptions [*Lipman*, 1997], but also due to magmatic or hydrothermal processes causing long-term subsidence [*Walker*, 1984] at otherwise dormant volcanoes.

[68] **Acknowledgments.** We appreciate fruitful discussions with Mehdi Nikkhoo and constructive and critical comments of reviewers on an earlier manuscript. This work was financially supported within the framework of the PROGRESS project funded by the German Ministry of Education and Research (BMBF), the Helmholtz Alliance "Remote Sensing and Earth System Dynamics," and the GFZ Potsdam. In addition, Holohan acknowledges a Marie-Curie International Mobility Fellowship cofunded by the Irish Research Council and Marie-Curie Actions. The data used were acquired by the European satellite *Envisat* and provided via the ESA proposal ID 3589 and 3455. RapidEye data were provided via the RESA proposal "Beobachtung von Vulkanen und deren Kopplung zu Erdbeben in Vorderasien." The photo of Tendürek volcano in Figure 2 was kindly provided by Grete Howard.

References

Anderson, E. (1936), The dynamics of the formation of cone sheets, ring dykes, and cauldron subsidence, *Proc. Indian Acad. Sci.*, *56*, 128–163.

Branney, M. J. (1995), Downsag and extension at calderas: new perspectives on collapse geometries from ice-melt, mining, and volcanic subsidence, *Bull. Volcanol.*, *57*(5), 303–318, doi:10.1007/s004450050096.

Byrne, P. K., B. van Wyk de Vries, J. B. Murray, and V. R. Troll (2009), The geometry of volcano flank terraces on Mars, *Earth Planet. Sci. Lett.*, *281*(1–2), 1–13, doi:10.1016/j.epsl.2009.01.043.

Byrne, P. K., E. P. Holohan, M. Kervyn, B. van Wyk de Vries, V. R. Troll, and J. B. Murray (2013), A sagging-spreading continuum of large volcano structure, *Geology*, *41*(3), 339–342, doi:10.1130/G33990.1.

Cayol, V., and F. H. Cornet (1998), Effects of topography on the interpretation of the deformation field of prominent volcanoes - Application to Etna, *Geophys. Res. Lett.*, *25*(11), 1979–1982.

Cecchi, E., B. Wyk de Vries, and J.-M. Lavest (2004), Flank spreading and collapse of weak-cored volcanoes, *Bull. Volcanol.*, *67*(1), 72–91, doi:10.1007/s00445-004-0369-3.

Chadwick, W. W., D. J. Geist, S. Jónsson, M. Poland, D. J. Johnson, and C. M. Meertens (2006), A volcano bursting at the seams: Inflation, faulting, and eruption at Sierra Negra volcano, Galápagos, *Geology*, *34*(12), 1025, doi:10.1130/G22826A.1.

Chen, C. W., and H. A. Zebker (2001), Two-dimensional phase unwrapping with use of statistical models for cost functions in nonlinear optimization, *J. Opt. Soc. Am. A*, *18*, 338–351.

Clough, C., H. Maufe, and E. Baley (1909), The cauldron subsidence of Glen-Coe, and the associated igneous phenomena, *Q. J. Soc. Lond.*, *65*, 611–678.

De Natale, G., C. Troise, F. Pingue, G. Mastrolorenzo, L. Pappalardo, M. Battaglia, and E. Boschi (2006), The Campi Flegrei caldera: unrest mechanisms and hazards, in *Mechanisms of Activity and Unrest at Large Calderas*, vol. *269*, pp. 25–45, Geological Society, London, U.K.

Dhont, D., and J. Chorowicz (2005), Review of the neotectonics of the Eastern Turkish–Armenian Plateau by geomorphic analysis of digital elevation model imagery, *Int. J. Earth Sci.*, *95*(1), 34–49, doi:10.1007/s00531-005-0020-3.

Doğan, B., and A. Karakaş (2013), Geometry of co-seismic surface ruptures and tectonic meaning of the 23 October 2011 Mw 7.1 Van earthquake (East Anatolian Region, Turkey), *J. Struct. Geol.*, *46*, 99–114, doi:10.1016/j.jsg.2012.10.001.

Dzurisin, D. (2007), *Volcano Deformation; Geodetic Monitoring Techniques*, Springer-Verlag, Berlin Heidelberg New York.

Ekström, G. (1994), Anomalous earthquakes on volcano ring-fault structures, *Earth Planet. Sci. Lett.*, *128*, 707–712.

Farr, T. G., et al. (2007), The shuttle radar topography mission, *Rev. Geophys.*, *45*(2005), 1–33, doi:10.1029/2005RG000183.

Ferretti, A., C. Prati, and F. Rocca (2001), Permanent Scatterers in SAR Interferometry, *IEEE Trans. Geosci. Rem. Sens.*, *39*(1), 8–20.

Fichtner, A., and H. Tkalčić (2010), Insights into the kinematics of a volcanic caldera drop: Probabilistic finite-source inversion of the 1996 Bárdarbunga, Iceland, earthquake, *Earth Planet. Sci. Lett.*, *297*(3–4), 607–615, doi:10.1016/j.epsl.2010.07.013.

Filson, J., T. Simkin, and L. Leu (1973), Seismicity of a caldera collapse: Galapagos Islands 1968, *J. Geophys. Res.*, *78*(35), 8591–8622, doi:10.1029/JB078i035p08591.

Geshi, N., T. Shimano, T. Chiba, and S. Nakada (2002), Caldera collapse during the 2000 eruption of Miyakejima Volcano, Japan, *Bull. Volcanol.*, *64*(1), 55–68, doi:10.1007/s00445-001-0184-z.

Goldstein, R. M., and C. L. Werner (1998), Radar interferogram filtering for geophysical applications, *Geophys. Res. Lett.*, *25*(21), 4035–4038.

Hanssen, R. F. (2001), *Radar Interferometry*, Kluwer Academic Publishers, Dordrecht, The Netherlands.

Holland, J. H. (1975), *Adaptation in Natural and Artificial Systems*, University of Michigan Press, Oxford, U.K.

Holohan, E. P., V. R. Troll, B. van Wyk de Vries, J. J. Walsh, and T. R. Walter (2008), Unzipping Long Valley: An explanation for vent migration patterns during an elliptical ring fracture eruption, *Geology*, *36*(4), 323, doi:10.1130/G24329A.1.

Holohan, E. P., M. P. J. Schöpfer, and J. J. Walsh (2011), Mechanical and geometric controls on the structural evolution of pit crater and caldera subsidence, *J. Geophys. Res.*, *116*, B07202, doi:10.1029/2010JB008032.

Holohan, E. P., T. R. Walter, M. P. J. Schöpfer, J. J. Walsh, B. V. W. De Vries, and V. R. Troll (2013), Origins of oblique-slip faulting during caldera subsidence, *J. Geophys. Res. Solid Earth*, *118*, 1778–1794, doi:10.1029/2012JB009560.

Hooper, A. (2006), Persistent scatterer radar interferometry for crustal deformation studies and modeling of volcanic deformation, Stanford University.

Hooper, A. (2008), A multi-temporal InSAR method incorporating both persistent scatterer and small baseline approaches, *Geophys. Res. Lett.*, *35*, L16302, doi:10.1029/2008GL034654.

Horasan, G., and A. Boztepe-Güney (2006), Observation and analysis of low-frequency crustal earthquakes in Lake Van and its vicinity, eastern Turkey, *J. Seismol.*, *11*(1), 1–13, doi:10.1007/s10950-006-9022-2.

Jones, R. H., and R. C. Stewart (1997), A method for determining significant structures in a cloud of earthquakes Simplifying the Earthquake Cloud, *J. Geophys. Res.*, *102*(134), 8245–8254.

Jónsson, S. (2009), Stress interaction between magma accumulation and trapdoor faulting on Sierra Negra volcano, Galápagos, *Tectonophysics*, *471*(1–2), 36–44, doi:10.1016/j.tecto.2008.08.005.

Jónsson, S., H. Zebker, P. Segall, and F. Amelung (2002), Fault Slip Distribution of the 1999 Mw 7.1 Hector Mine, California, Earthquake, Estimated from Satellite Radar and GPS Measurements, *Bull. Seismol. Soc. Am.*, *92*(4), 1377–1389, doi:10.1785/0120000922.

Kampes, B., and S. Usai (1999), Doris: The Delft object-oriented radar interferometric software, in *paper presented at 2nd Operationalization of Remote Sensing Symposium, ITC*, Enschede, The Netherlands.

Karakhanian, A., R. Djrbashian, V. Trifonov, H. Philip, S. Arakelian, and A. Avagian (2002), Holocene-historical volcanism and active faults as natural risk factors for Armenia and adjacent countries, *J. Volcanol. Geotherm. Res.*, *113*(1–2), 319–344, doi:10.1016/S0377-0273(01)00264-5.

Karakhanian, A. S., et al. (2004), Active faulting and natural hazards in Armenia, eastern Turkey and northwestern Iran, *Tectonophysics*, *380*(3–4), 189–219, doi:10.1016/j.tecto.2003.09.020.

Konstantinou, K. I., H. Kao, C. Lin, and W. Liang (2003), Analysis of broadband regional waveforms of the 1996 September 29 earthquake at Bárdarbunga volcano, central Iceland : investigation of the magma injection hypothesis, *Geophys. J. Int.*, *154*, 134–145.

Kumagai, H., T. Ohminato, M. Nakano, M. Ooi, A. Kubo, H. Inoue, and J. Oikawa (2001), Very-long-period seismic signals and caldera formation at Miyake Island, Japan, *Science (New York, N.Y.)*, *293*(5530), 687–90, doi:10.1126/science.1062136.

Lipman, P. W. (1997), Subsidence of ash-flow calderas: relation to caldera size and magma-chamber geometry, *Bull. Volcanol.*, *59*(3), 198–218, doi:10.1007/s004450050186.

Michon, L., T. Staudacher, V. Ferrazzini, P. Bachèlery, and J. Marti (2007), April 2007 collapse of Piton de la Fournaise: A new example of caldera formation, *Geophys. Res. Lett.*, *34*, L21301, doi:10.1029/2007GL031248.

Mori, J., and C. McKee (1987), Outward-dipping ring-fault structure at rabaul caldera as shown by earthquake locations, *Science (New York, N.Y.)*, *235*(4785), 193–195, doi:10.1126/science.235.4785.193.

Nairn, I., C. McKee, B. Talai, and C. Wood (1995), Geology and eruptive history of the Rabaul Caldera area, Papua New Guinea, *J. Volcanol. Geotherm. Res.*, *69*, 255–284.

Okada, Y. (1985), Surface deformation due to shear and tensile faults in a half-space, *Bull. Seismol. Soc. Am.*, *75*(4), 1135–1154, doi:10.1016/0148-9062(86)90674-1.

Ölmez, E., T. Ercan, and T. Yildirim (1994), Volcanology and Geothermal Energy possibilities of the Tendürek Area (Diyadin, Zilan, Caldıran), Eastern Anatolia (Turkey), in *47. Türkeiye Jeoloji Kurultay Bildiri Özleri Kitabi 1994*, pp. 106–107.

Oruc, N. (2008), Occurrence and problems of high fluoride waters in Turkey: an overview, *Environ. Geochem. Health*, *30*(4), 315–23, doi:10.1007/s10653-008-9160-2.

Reilinger, R., et al. (2006), GPS constraints on continental deformation in the Africa-Arabia-Eurasia continental collision zone and implications for the dynamics of plate interactions, *J. Geophys. Res.*, *111*(B5), 1–26, doi:10.1029/2005JB004051.

Roche, O., T. H. Druitt, and O. Merle (2000), Experimental study of caldera formation, *J. Geophys. Res.*, *105*(B1), 395–416, doi:10.1029/1999JB900298.

Rosen, P., S. Henley, G. Peltzer, and M. Simons (2004), Updated Repeat Orbit Interferometry Package Released, *Eos. Trans. AGU*, *85*(5), 47.

Ruch, J., and T. R. Walter (2010), Relationship between the InSAR-measured uplift, the structural framework, and the present-day stress field at Lazufre volcanic area, central Andes, *Tectonophysics*, *492*(1–4), 133–140, doi:10.1016/j.tecto.2010.06.003.

Rytuba, J. J. (1994), Evolution of volcanic and tectonic features in caldera settings and their importance in localization of ore deposits, *Econ. Geol.*, *89*(8), 1687–1696, doi:10.2113/gsecongeo.89.8.1687.

Sambridge, M., and K. Mosegaard (2002), Monte Carlo Methods in Geophysical Inverse Problems, *Rev. Geophys.*, *40*(3), 1009, doi:10.1029/2000RG00089.

Saunders, S. (2001), The shallow plumbing system of Rabaul caldera: a partially intruded ring fault?, *Bull. Volcanol.*, *63*(6), 406–420, doi:10.1007/s004450100159.

Scarpati, C., P. Cole, and A. Perrotta (1993), The Neapolitan Yellow Tuff - A large volume multiphase eruption from Campi Flegrei, Southern Italy, *Bull. Volcanol.*, *55*, 343–356.

Shirzaei, M., T. R. Walter, and R. Bürgmann (2013), Coupling of Hawaiian volcanoes only during overpressure condition, *Geophys. Res. Lett.*, *40*, 1994–1999, doi:10.1002/grl.50470.

Shuler, A., G. Ekström, and M. Nettles (2013), Physical mechanisms for vertical-CLVD earthquakes at active volcanoes, *J. Geophys. Res. Solid Earth*, *118*, 1–18, doi:10.1002/jgrb.50131.

Sigmundsson, F., H. Vadon, and D. Massonnet (1997), Readjustment of the Krafla Spreading Segment to crustal rifting measured by satellite radar interferometry, *Geophys. Res. Lett.*, *24*(15), 1843–1846, doi:10.1029/97GL01934.

Sigurdsson, H. (2000), The history of volcanology, in *Encyclopedia of volcanoes*, pp. 15–37, Academic Press, London, U.K.

Simkin, T., and K. A. Howard (1970), Caldera Collapse in the Galapagos Islands, 1968, *Science*, *169*(3944), 429–437.

Simkin, T., and L. Siebert (2002), Volcanoes of the World: an Illustrated Catalog of Holocene Volcanoes and their Eruptions, Smithsonian Institution, Global Volcanism Program Digital Information Series, GVP-3,

Sudhaus, H., and S. Jónsson (2009), Improved source modelling through combined use of InSAR and GPS under consideration of correlated data errors: application to the June 2000 Kleifarvatn earthquake, Iceland, *Geophys. J. Int.*, *176*(2), 389–404, doi:10.1111/j.1365-246X.2008.03989.x.

Tolluoglu, D. (2006), Monitoring deformations on Tendürek volcano by differential SAR interferometry, Van Yuzuncu Yil University.

Walker, G. P. L. (1984), Downsag calderas, ring faults, caldera sizes, and incremental caldera growth, *J. Geophys. Res.*, *89*(B10), 8407–8416, doi:10.1029/JB089iB10p08407.

Wilson, C. J. N., and W. Hildreth (1997), The Bishop Tuff : New Insights from Eruptive Stratigraphy 1, *J. Geol.*, *105*, 407–439.

Wright, T. J. (2003), Source model for the M w 6.7, 23 October 2002, Nenana Mountain Earthquake (Alaska) from InSAR, *Geophys. Res. Lett.*, *30*(18), 1974, doi:10.1029/2003GL018014.

Yang, X.-M., P. M. Davis, and J. H. Dieterich (1988), Deformation From Inflation of a Dipping Finite Prolate Spheroid in an Elastic Half-Space as a Model for Volcanic Stressing, *J. Geophys. Res.*, *93*, 4249–4257.

Yılmaz, Y., Y. Guner, and F. Şaroğlu (1998), Geology of the quaternary volcanic centres of the east Anatolia, *J. Volcanol. Geotherm. Res.*, *85*(1–4), 173–210, doi:10.1016/S0377-0273(98)00055-9.

Yun, S., P. Segall, and H. Zebker (2006), Constraints on magma chamber geometry at Sierra Negra Volcano, Galápagos Islands, based on InSAR observations, *J. Volcanol. Geotherm. Res.*, *150*(1–3), 232–243, doi:10.1016/j.jvolgeores.2005.07.009.